Saarakkala, Seppo E.; Sokolov, Maksim; Hosseinzadeh, Reza; Hinkkanen, Marko

Levitation control for a double-sided bearingless linear motor based on feedback linearization

Published in:
Proceedings of the 11th IEEE Energy Conversion Congress and Exposition, ECCE 2019

DOI:
10.1109/ECCE.2019.8913219

Published: 29/09/2019

Document Version
Peer-reviewed accepted author manuscript, also known as Final accepted manuscript or Post-print

Please cite the original version:
Saarakkala, S. E., Sokolov, M., Hosseinzadeh, R., & Hinkkanen, M. (2019). Levitation control for a double-sided bearingless linear motor based on feedback linearization. In *Proceedings of the 11th IEEE Energy Conversion Congress and Exposition, ECCE 2019* (pp. 4923-4930). (IEEE Energy Conversion Congress and Exposition). IEEE. https://doi.org/10.1109/ECCE.2019.8913219

Levitation Control for a Double-Sided Bearingless Linear Motor Based on Feedback Linearization

Seppo E. Saarakkala, Maksim Sokolov, Reza Hosseinzadeh, and Marko Hinkkanen
Aalto University School of Electrical Engineering, P.O. Box 15500, FI-00076 Aalto, Espoo, Finland

***Abstract*—This paper deals with levitation control for a double-sided bearingless linear-motor system. Analytical design rules for a state-feedback gain and a state observer are derived. To decouple the production of forces in thrust- and normal-force directions, feedback-linearizing control based on the magnetic model is proposed. The proposed control design is tested in an experimental system consisting of four individually supplied linear-motor units in a double-sided configuration. The results from time-domain simulations and experimental tests suggest that the proposed control design can successfully provide smooth transition to contactless operation and retain the stable levitation during the movement in the thrust-force direction.**

***Index Terms*—Bearingless, control, levitation, linear motor.**

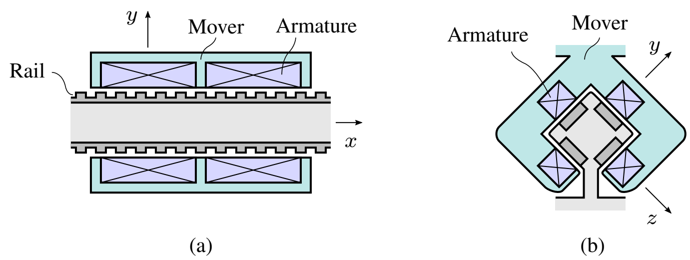

Fig. 1. Example configuration of a bearingless linear motor system, consisting of a beam with rails and a mover with eight motor units: (a) cross-section in the xy plane; (b) cross-section in the yz plane.

I. Introduction

A linear motor system is an attractive alternative as a propulsion source for various applications requiring linear movement, such as urban rail transit [1], wave-energy generation [2], electromagnetic launch systems [3], [4], machine tools [5], and elevator systems [6], [7]. In addition to the thrust force, linear machines also produce a normal force component. As depicted in Fig. 1, a bearingless linear motor system can be formed, when several individually controlled motor units are arranged, e.g., in a two-sided or four-sided configuration. The thrust and normal forces of the individual motor units are controlled to create the required linear motion and the remaining degrees of freedom are stabilized with an active levitation control.

Active levitation control is a widely studied subject in the field of active magnetic bearings (AMBs). Several different control structures have been proposed for AMB control, simple proportional-integral-derivative (PID) controller being the most common one [8]. The nonlinearities of the electromagnetic force actuator (e.g., magnetic saturation of the iron core and the voltage saturation of the supply device) as well as the structural bending modes of the rotor cause the major challenges, making the simple PID levitation controller sometimes an inadequate choice. Therefore, the AMBs are often treated as systems with uncertainties and robust-control-theory design tools are applied [8], [9]. Alternatively, if the force actuator nonlinearities are known, feedback linearization is a powerful tool to tackle them [10]. State-feedback control methods, on the other hand, may be applied to controlling the bending modes of the rotor [11], [12].

In contrast with control of conventional motors equipped with the AMBs, levitation control of bearingless motors (linear or rotating) has an additional challenge: the force production in the traction and levitation directions becomes coupled, because the magnetic circuit is shared. Decoupling methods have been proposed, e.g. [13], [14], but only a few of these methods take properly into account both the effects of magnetic saturation and airgap variation [14]. Moreover, systematic design rules for levitation control of bearingless motors are not available, apart from a recent work [15]. However, the levitation control design in [15] is based on applying a linear motor model. Instead of systematically synthesizing the levitation control system, proportional-derivative (PD) or PID controllers, with trial-and-error tuning, are used [13], [16]–[18].

This paper proposes a feedback-linearization state-space levitation control method for a double-sided bearingless linear motor drive. The main contributions can be summarized as follows:

1) Analytical design rules for the levitation controller (including the feedback gain and the state observer) are presented.
2) A feedback-linearization structure, based on the magnetic model of the motor, is developed. This structure decouples the thrust- and normal-force production and makes the levitation-control loop independent of the inner force-control loops.
3) Robustness against parameter errors and sensitivity to measurement noise is analyzed by means of time-domain simulations.

A similar control structure is applied in the simulation study [19], but analytical design rules for the controller gains are not provided. The developed controllers is experimentally evaluated with a system consisting of four 2-kW linear flux-switching permanent-magnet (FSPM) motor units in a double-sided configuration.

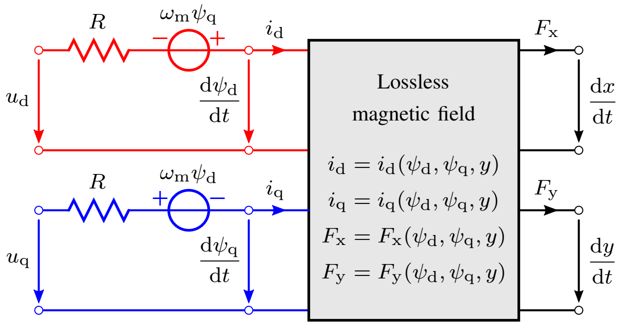

Fig. 2. Electrical dynamics of an FSPM motor unit modelled in dq coordinates, rotating at $\omega_m = (2\pi/\tau) \cdot dx/dt$.

II. Modeling of an FSPM Linear Motor System

A. Electrical Subsystem

Fig. 2 shows the lumped-element dynamic model of an FSPM motor unit in dq coordinates [20]. The voltage equations in dq coordinates are

$$\frac{d\psi_d}{dt} = u_d - Ri_d + \omega_m\psi_q \tag{1a}$$
$$\frac{d\psi_q}{dt} = u_q - Ri_q - \omega_m\psi_d \tag{1b}$$

where ψ_d, ψ_q are the flux-linkage components, u_d, u_q are the voltage components, R is the resistance, $\omega_m = (2\pi/\tau) \cdot dx/dt$ is the electrical angular speed, and τ is the pole pitch of the rail. As shown, e.g. in [20], the currents can be modeled as functions of the flux linkages and the airgap y,

$$i_d = i_d(\psi_d, \psi_q, y) \qquad i_q = i_q(\psi_d, \psi_q, y) \tag{2}$$

Alternatively, the reciprocal relationships $\psi_d = \psi_d(i_d, i_q, y)$ and $\psi_q = \psi_q(i_d, i_q, y)$ could be used. These functions are generally nonlinear because of the magnetic saturation.

In accordance with Fig. 2, the rate of change of the magnetic field energy is

$$\frac{dW}{dt} = \left(i_d\frac{d\psi_d}{dt} + i_q\frac{d\psi_q}{dt}\right) + \frac{2\pi}{\tau}(\psi_d i_q - \psi_q i_d)\frac{dx}{dt} - F_x\frac{dx}{dt} - F_y\frac{dy}{dt} \tag{3}$$

The thrust force and the normal force, respectively, are

$$F_x = F_x(\psi_d, \psi_q, y) = \frac{2\pi}{\tau}(\psi_d i_q - \psi_q i_d) \tag{4a}$$
$$F_y = F_y(\psi_d, \psi_q, y) = -\frac{\partial W}{\partial y} \tag{4b}$$

Naturally, the airgap y can change in bearingless motors. Alternatively, the forces may be expressed as functions of the currents as $F_x = F_x(i_d, i_q, y)$ and $F_y = F_y(i_d, i_q, y)$. If spatial harmonics were taken into account, the currents and forces would depend on the position x as well.

B. Mechanical Subsystem

The mechanical configuration is shown in Fig. 3(a). A rigid mechanical structure is assumed. The rotational movements around the x and y directions are mechanically prevented, and the rotational movement around the z direction is neglected. The actuators in the upper section (units 1 and 2) and in the lower section (units 3 and 4) are assumed to be identical and decoupled. Therefore, the model is considered for the upper section only. The motion equations in the x direction are

$$m\frac{dv_x}{dt} = \Sigma F_x + F_{x,d} \qquad \frac{dx}{dt} = v_x \tag{5}$$

where v_x is the linear velocity, $\Sigma F_x = F_{x1} + F_{x2}$ is the thrust force, $F_{x,d}$ is the external disturbance force (which includes the gravitational force $-mg$ and other external forces affecting in the x direction), and m is the mass (half the total mass of the mover). The motion equations in the y direction are

$$m\frac{dv_y}{dt} = \Delta F_y + F_{y,d} \qquad \frac{d\Delta y}{dt} = v_y \tag{6}$$

where v_y is the linear velocity, $\Delta y = (y_1 - y_2)/2$ is the differential airgap, $\Delta F_y = F_{y2} - F_{y1}$ is the differential normal force, and $F_{y,d}$ is the external disturbance force. The overall system is nonlinear due to the force expressions (4). Furthermore, the open-loop system is unstable in the y direction.

III. Levitation Control System

Fig. 3(b) shows the overall structure of the controller applied for the upper section. The levitation controllers for the upper and lower sections are identical and independent of each other. The cascaded control system includes the inner and outer control loops and a decoupling block between them. The levitation controller drives the measured differential airgap Δy to zero using the differential normal force ΔF_y. The traction controller provides the total thrust force reference, which is equally shared between the motor units.

A. Feedback Linearization and Decoupling

For given $\Sigma F_{x,ref}$, $\Delta F_{y,ref}$, Δy, and F_0, the force references for each motor unit are

$$F_{x1,ref} = F_{x2,ref} = \Sigma F_{x,ref}/2 \tag{7a}$$
$$F_{y1,ref} = F_0 - \Delta F_{y,ref}/2 \tag{7b}$$
$$F_{y2,ref} = F_0 + \Delta F_{y,ref}/2 \tag{7c}$$

where F_0 is a common-mode attraction-force component, and it can be arbitrarily selected within the boundaries of the maximum motor current. If the static nonlinearities in (2) and (4) are known, the flux linkages of each motor unit can be solved as functions of the force references and the airgap. Using (2), the flux references are finally mapped to the current references, which are fed to the current controllers, as shown in Fig. 3(b). The system seen by the traction and levitation controllers becomes linear and decoupled.

The nonlinear functions in (2) and (4) can be determined, e.g., by completing a series of static finite-element-method

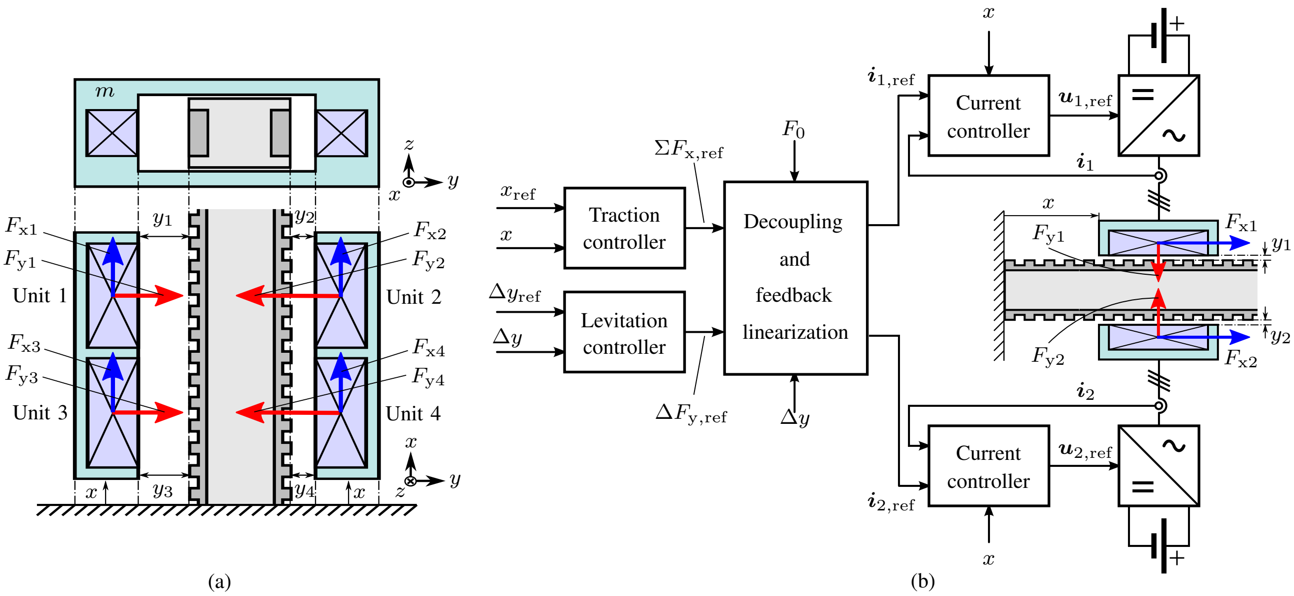

Fig. 3. (a) Mechanical configuration of the double-sided linear bearingless machine consisting of four individual motor units. (b) Traction and levitation controllers for the upper section (motor units 1 and 2). The decoupling and feedback linearization block includes a nonlinear mapping from the force references and airgap positions to the current references. The upper and lower sections share the same traction controller. The lower section has its own levitation controller.

(FEM) simulations and storing the results in the form of look-up tables. Alternatively, explicit functions can be used [20]. The design of the feedback linearization is discussed in more detail in Section IV-B.

B. State Feedback Control

A hold-equivalent exact discrete-time state-space representation of (6) is

$$\begin{aligned} \boldsymbol{x}_\mathrm{s}(k+1) &= \boldsymbol{A}\boldsymbol{x}_\mathrm{s}(k) + \boldsymbol{B}\Delta F_\mathrm{y}(k) + \boldsymbol{B}F_\mathrm{y,d}(k) \\ \Delta y(k) &= \boldsymbol{C}\boldsymbol{x}_\mathrm{s}(k) \end{aligned} \tag{8}$$

where $\boldsymbol{x}_\mathrm{s} = [v_\mathrm{y}, \Delta y]^\mathrm{T}$ is the state vector and $F_\mathrm{y,d}$ is the external disturbance force. The system matrices are

$$\boldsymbol{A} = \begin{bmatrix} 1 & 0 \\ T_\mathrm{s} & 1 \end{bmatrix} \quad \boldsymbol{B} = \begin{bmatrix} \frac{T_\mathrm{s}}{m} \\ \frac{T_\mathrm{s}^2}{2m} \end{bmatrix} \quad \boldsymbol{C} = \begin{bmatrix} 0 & 1 \end{bmatrix} \tag{9}$$

where T_s is the sampling interval. As shown in Fig. 4, a state-feedback control law is used

$$\Delta F'_\mathrm{y,ref}(k) = -\boldsymbol{K}\boldsymbol{x}_\mathrm{s}(k) + k_\mathrm{I}\Delta y_\mathrm{I}(k) \tag{10}$$

where $\boldsymbol{K} = [k_1, k_2]$ and k_I are the feedback gains. The integral state is defined as

$$\begin{aligned} \Delta y_\mathrm{I}(k+1) = \Delta y_\mathrm{I}(k) + \Delta y_\mathrm{ref}(k) - \boldsymbol{C}\boldsymbol{x}_\mathrm{s}(k) \\ + \frac{1}{k_2}[\Delta F_\mathrm{y,ref}(k) - \Delta F'_\mathrm{y,ref}(k)] \end{aligned} \tag{11}$$

where the limited differential-force reference $\Delta F_\mathrm{y,ref}$ can be calculated as a function Δy and the given maximum d-axis current $i_\mathrm{d,max}$ using (16). In the linear operation region, the augmented closed-loop system is

$$\begin{aligned} \begin{bmatrix} \boldsymbol{x}_\mathrm{s}(k+1) \\ \Delta y_\mathrm{I}(k+1) \end{bmatrix} &= \underbrace{\begin{bmatrix} \boldsymbol{A} - \boldsymbol{B}\boldsymbol{K} & \boldsymbol{B}k_\mathrm{I} \\ -\boldsymbol{C} & 1 \end{bmatrix}}_{\boldsymbol{A}_\mathrm{cl}} \begin{bmatrix} \boldsymbol{x}_\mathrm{s}(k) \\ \Delta y_\mathrm{I}(k) \end{bmatrix} \\ &+ \begin{bmatrix} \boldsymbol{0} \\ 1 \end{bmatrix} \Delta y_\mathrm{u,ref}(k) + \begin{bmatrix} \boldsymbol{B} \\ 0 \end{bmatrix} F_\mathrm{y,d}(k) \end{aligned} \tag{12}$$

The characteristic polynomial of the closed-loop system is $B_\mathrm{fb}(z) = \det(z\mathbf{I} - \boldsymbol{A}_\mathrm{cl})$. Here, the three poles are divided into a real pole and a pair of complex poles, $B_\mathrm{fb}(z) = (z+a)(z^2+bz+c)$, leading to the following feedback gains

$$\begin{aligned} k_1 &= m\frac{a-b+c+7}{4T_\mathrm{s}} \qquad k_2 = m\frac{3a+b-c+5}{2T_\mathrm{s}^2} \\ k_\mathrm{I} &= m\frac{a+b+c+1}{T_\mathrm{s}^2} \end{aligned} \tag{13}$$

C. State Observer

The state-feedback control law requires information both from the differential airgap Δy and from the linear velocity v_y, but only the differential airgap is available as a feedback signal. The velocity v_y could be calculated as a direct differentiation of the measured differential airgap, $v_\mathrm{y}(k) = [\Delta y(k) - \Delta y(k-1)]/T_\mathrm{s}$, but this approach is very noise sensitive. A more elaborate solution is to use a full-order state observer to estimate the state vector as

$$\begin{aligned} \hat{\boldsymbol{x}}_\mathrm{s}(k+1) = \boldsymbol{A}\hat{\boldsymbol{x}}_\mathrm{s}(k) + \boldsymbol{B}\Delta F_\mathrm{y,ref}(k) \\ + \boldsymbol{L}[\Delta y(k) - \boldsymbol{C}\hat{\boldsymbol{x}}_\mathrm{s}(k)] \end{aligned} \tag{14}$$

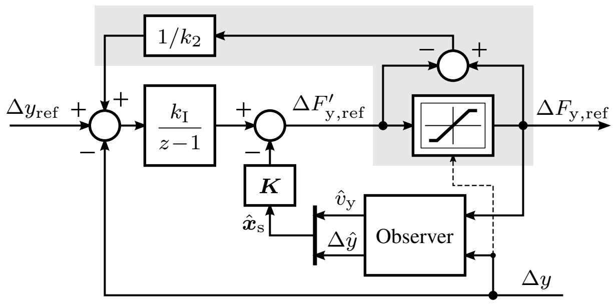

Fig. 4. Levitation controller. The discrete-time state-space controller consists of an integrator, a state feedback and a state observer. The shaded area shows limitation of the force reference and a back-calculation anti-windup mechanism. The maximum force is determined based on (16) using the maximum d-axis current and Δy.

TABLE I
PARAMETERS OF THE LEVITATION CONTROL SYSTEM

Current control	
d-axis inductance L_{d}	100 mH
q-axis inductance L_{q}	100 mH
Closed-loop bandwidth α_{c}	$2\pi \cdot 700$ rad/s
Sampling time T_{sc}	62.5 μs
Feedback linearization	
Nominal airgap y_{N}	1.05 mm
Current stiffness k_{x}	70 N/A
Current stiffness k_{y}	130 N/A
Force coefficient f_{y}	6.0 kN
Force coefficient c_{y}	0.3 1/mm
Levitation control	
Total mass of the mover $2m$	100 kg
Real-valued control pole a_{p}	$2\pi \cdot 5$ rad/s
Natural frequency of the complex control poles ω_{s}	$2\pi \cdot 50$ rad/s
Damping of the complex control poles ζ_{s}	0.8
Natural frequency of the complex observer poles ω_{o}	$2\pi \cdot 250$ rad/s
Damping of the complex observer poles ζ_{o}	0.8
Sampling time T_{s}	125 μs

where $\boldsymbol{L} = [l_1, l_2]^{\mathrm{T}}$ is the observer gain. The observer gain is defined by the desired second-order characteristic polynomial, $B_{\mathrm{o}}(z) = \det(z\mathbf{I} - \boldsymbol{A} + \boldsymbol{LC}) = z^2 + dz + e$, giving

$$l_1 = (e + d + 1)/T_{\mathrm{s}} \qquad l_2 = d + 2 \tag{15}$$

IV. Control Design Example

This section provides a design example for the proposed levitation controller. The most important aspects related to the implementation and parametrization of the control system are covered. The system parameters are collected in Table I.

A. Experimental System

The experimental setup used in this example is shown in Fig. 5, and it consists of four three-phase linear FSPM motor units, corresponding to Fig. 3. Each motor unit is supplied with an individual three-phase inverter and equipped with sensors for measuring the airgap length and the linear position on the rail. Furthermore, the phase currents and the DC-link voltage of each unit are measured for the current control loops.

Fig. 5. Experimental setup.

B. Feedback Linearization

The force production of an FSPM motor unit is analyzed by means of static FEM simulations. The current components $(i_{\mathrm{d}}, i_{\mathrm{q}})$ and the force components $(F_{\mathrm{x}}, F_{\mathrm{y}})$ were solved as a function of the flux linkages and airgap $(\psi_{\mathrm{d}}, \psi_{\mathrm{q}}, y)$ in predefined operating points. The operating points were chosen to cover the whole operating range of the motor in terms of allowable currents and possible airgap variation [20].

Based on the FEM analysis, the forces in (4) are approximated in this paper as

$$F_{\mathrm{x}} = k_{\mathrm{x}} i_{\mathrm{q}} \tag{16a}$$

$$F_{\mathrm{y}} = -k_{\mathrm{y}} i_{\mathrm{d}} - \underbrace{\frac{f_{\mathrm{y}}}{(1 + c_{\mathrm{y}} y)^2}}_{f_0(y)} \tag{16b}$$

where k_{x} and k_{y} are the force-actuator current stiffnesses, $f_0(y)$ is the normal force caused by the permanent magnets only, and c_{y} and f_{y} are force coefficients. The normal-force references $F_{\mathrm{y1,ref}}$ and $F_{\mathrm{y2,ref}}$ of the motor units from (7) are mapped to the current references using (16),

$$i_{\mathrm{d1,ref}} = -\frac{F_0(\Delta y) - \Delta F_{\mathrm{y,ref}}/2 + f_{01}(y_1)}{k_{\mathrm{y}}} \tag{17a}$$

$$i_{\mathrm{d2,ref}} = -\frac{F_0(\Delta y) + \Delta F_{\mathrm{y,ref}}/2 + f_{02}(y_2)}{k_{\mathrm{y}}} \tag{17b}$$

$$i_{\mathrm{q1,ref}} = i_{\mathrm{q2,ref}} = \frac{\Sigma F_{\mathrm{x,ref}}}{2k_{\mathrm{x}}} \tag{17c}$$

where $f_{01}(y_1)$ and $f_{02}(y_2)$ are the normal forces of motor units 1 and 2, respectively, caused by the permanent magnets only.

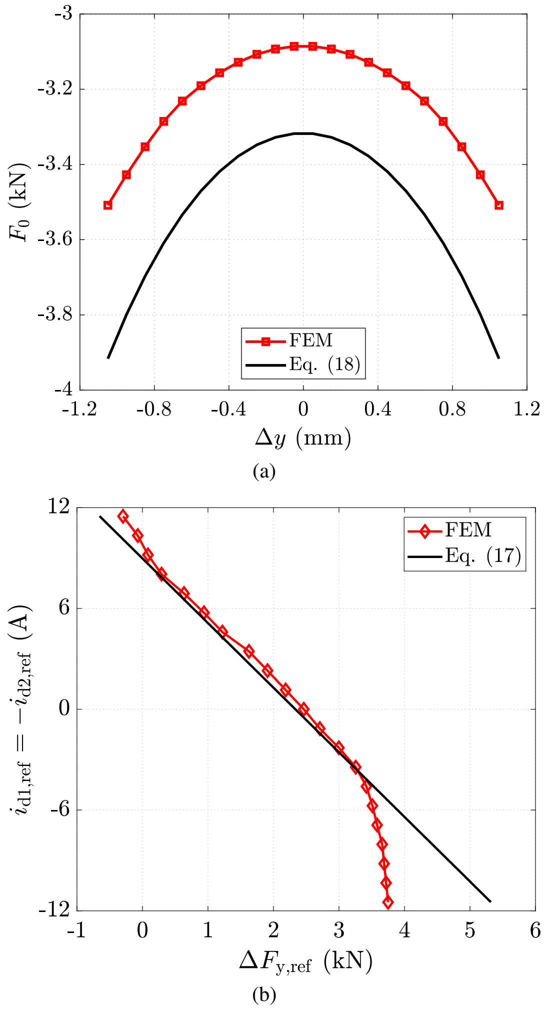

Fig. 6. (a) Common-mode attraction force F_0 as a function of differential airgap Δy. (b) d-axis current references as a function of differential force $\Delta F_{\mathrm{y,ref}}$ at Δy = 0.7 mm.

Here, the common-mode normal-force component is selected as

$$F_0(\Delta y) = -\frac{f_{01}(y_1) + f_{02}(y_2)}{2} \tag{18}$$

which results in the control strategy where $i_{\mathrm{d1,ref}} = -i_{\mathrm{d2,ref}}$.

To evaluate the accuracy of the simplified feedback linearization, Fig. 6 compares the numerical values obtained from (17) and (18) to the corresponding FEM results. As an example, Fig. 6(a) shows the common-mode attraction force F_0 as a function of Δy, and Fig. 6(b) shows the d-axis current references as a function of differential force $\Delta F_{\mathrm{y,ref}}$ at Δy = 0.7 mm. Fig. 6 confirms that the approximate model in (16) matches reasonably well with the FEM results, when the control strategy (18) is chosen. Even if the force approximation in (16b) is slightly inaccurate, the integral action of the levitation controller (11) compensates for the modeling errors seen in Fig. 6. If a better accuracy is required, feedback linearization could be directly implemented in the form of look-up tables based on the static FEM data.

For the inner control loops, cf. Fig. 3(b), identical proportional-integral (PI) current controllers are applied for all four motor units. Their tuning is based on the internal model control (IMC) principle [21]. If the current-control bandwidth α_{c} is chosen significantly higher (preferably more than ten times) than the approximate levitation-control bandwidth, the current references (17) can be realized fast enough.

C. Considerations for Pole Placement

Because the state vector consists of two states and the controller is augmented with the integrator, the closed-loop system (12) is of the third order. Furthermore, the full-order observer increases the order of the levitation control system by two, i.e., five poles in total have to be placed. The desired characteristic polynomial in the discrete-time domain is $B(z) = (z + a)(z^2 + bz + c)(z^2 + dz + e)$. However, it is easier to choose the pole locations in the continuous-time domain, where the corresponding polynomial is

$$B(s) = (s + a_{\mathrm{p}})(s^2 + b_{\mathrm{c}}s + c_{\mathrm{c}})(s^2 + d_{\mathrm{c}}s + e_{\mathrm{c}}) \tag{19}$$

The complex-conjugate poles of $s^2 + b_{\mathrm{c}}s + c_{\mathrm{c}} = s^2 + 2\zeta_{\mathrm{s}}\omega_{\mathrm{s}}s + \omega_{\mathrm{s}}^2$ are treated as faster poles (related to the speed-control loop). If $0.6 < \zeta_{\mathrm{s}} < 0.9$ is selected, ω_{s} represents the approximate -3 dB bandwidth of the speed-control loop. The real-valued pole $s = -a_{\mathrm{p}}$ represents the airgap regulation dynamics, a_{p} being the approximate -3 dB bandwidth. The remaining polynomial $s^2 + d_{\mathrm{c}}s + e_{\mathrm{c}} = s^2 + 2\zeta_{\mathrm{o}}\omega_{\mathrm{o}}s + \omega_{\mathrm{o}}^2$ is related to the observer poles. The following rough guidelines can be used to set the bandwidths

$$\begin{aligned} &\alpha_{\mathrm{c}} < \pi/(10T_{\mathrm{sc}}) \qquad \omega_{\mathrm{s}} < \alpha_{\mathrm{c}}/10 \\ &2\omega_{\mathrm{s}} < \omega_{\mathrm{o}} < \alpha_{\mathrm{c}}/2 \qquad a_{\mathrm{p}} < \omega_{\mathrm{s}}/10 \end{aligned} \tag{20}$$

where T_{sc} is the sampling interval of the current-control loop. It is worth mentioning that the selection of ω_{o} is a compromise between the measurement-noise amplification and the effect of the observer on the dynamic response of the overall control system. If the noise content in the position measurement is low, a high value for ω_{o} can be selected and the observer has negligible effect on the control performance. Furthermore, if the rail beam has a structural bending mode in a low-frequency region, it is advisable to relocate the control poles such that $\omega_{\mathrm{s}} < 5\omega_{\mathrm{r}}$, where ω_{r} is the predicted natural resonant frequency of the bending mode. Table I gives the numerical values for the selected design parameters.

The continuous-time coefficients are mapped to their exact discrete-time equivalents as

$$\begin{aligned} &a = -\mathrm{e}^{-a_{\mathrm{p}}T_{\mathrm{s}}} \qquad c = \mathrm{e}^{-b_{\mathrm{c}}T_{\mathrm{s}}} \qquad e = \mathrm{e}^{-d_{\mathrm{c}}T_{\mathrm{s}}} \\ &b = -2\mathrm{e}^{-b_{\mathrm{c}}T_{\mathrm{s}}/2}\cos\left(T_{\mathrm{s}}\sqrt{c_{\mathrm{c}} - b_{\mathrm{c}}^2/4}\right) \\ &d = -2\mathrm{e}^{-d_{\mathrm{c}}T_{\mathrm{s}}/2}\cos\left(T_{\mathrm{s}}\sqrt{e_{\mathrm{c}} - d_{\mathrm{c}}^2/4}\right) \end{aligned} \tag{21}$$

and the corresponding controller gains are calculated using (13) and (15).

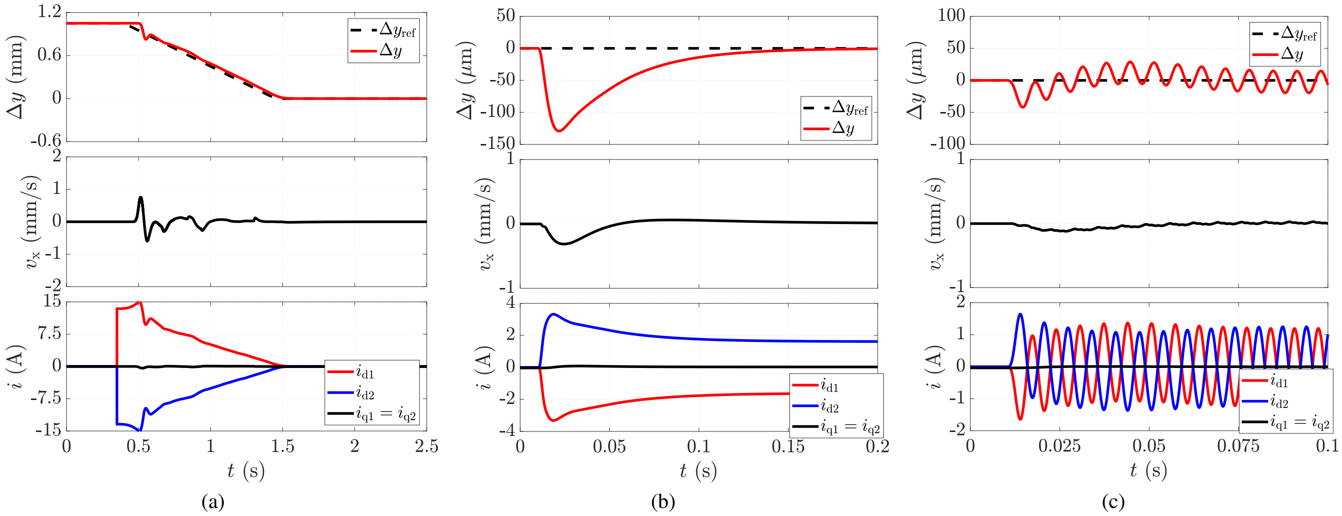

Fig. 7. Simulation results showing the operation of the proposed levitation control system: (a) reference tracking dynamics; (b) stepwise disturbance-force rejection; (c) sinusoidal disturbance-force rejection. In each subfigure, the first subplot shows the measured differential airgap Δy and its reference Δy_{ref}, the second subplot shows the measured x-direction position and velocity, and the last subplot shows the measured currents of the motor units.

D. Traction Control

Since traction control is not the main topic of this paper, a cascaded structure consisting of a proportional position controller and a PI speed controller is applied. Traction control is parametrized to have slower dynamics than levitation control. Furthermore, a counterweight is mounted to the system to compensate for the gravitational force acting on the mover.

V. Results

In this section, the proposed levitation control system is evaluated by means of time-domain simulations and experimental tests. The experiments were carried out using the test system shown in Fig. 5. The robustness of the control system against parameter errors and sensitivity to measurement noise is analyzed by means of time-domain simulations.

A. Time-Domain Simulations

In the simulation plant model, the electrical subsystems of two FSPM motor units are modeled using the voltage equations (1) together with the nonlinear mappings from the flux linkages to the currents, (2), and from the flux linkages to the forces, (4). These mappings are implemented in the form of look-up tables, and they are based directly on the numerical data from the FEM analysis (without any approximations or simplifications). The mechanical subsystem is modeled using (5) and (6), where only the upper section is considered. The absolute airgaps of the two motor units are defined as $y_1 = y_{\mathrm{N}} + \Delta y$ and $y_2 = y_{\mathrm{N}} - \Delta y$. The x direction movement of the two motor units is assumed to be perfectly aligned, i.e., $x_1 = x_2$. The levitation control system [cf. Fig. 3(b)] is implemented according to the design guidelines and parameter values given in Section IV.

Fig. 7 shows a set of simulation results for the proposed levitation controller. Fig. 7(a) shows the initial start-up of the levitation. Motor unit 2 is initially attached to the rail and the active levitation starts at $t = 0.3$ s. Even if the approximate model (16) is used for feedback linearization, the reference tracking accuracy of levitation control is still in an acceptable level. It can be seen that the levitation controller provides smooth and fast transition to a stable levitation mode. Fig. 7(b) shows the response for a stepwise external disturbance force $F_{\mathrm{y,d}} = 500$ N, applied at $t = 0.01$ s. It can be seen that the system fully rejects the stepwise disturbance force, and the maximum deviation in Δy during the disturbance step is less than 15% of the nominal airgap. Fig. 7(c) shows the response for a sinusoidal external disturbance force $F_{\mathrm{y,d}}$ (having the amplitude of 500 N and the frequency of 150 Hz), which is applied at $t = 0.01$ s. The deviation in Δy in the steady state is less than 50 μm peak-to-peak, which is less than 5% of the nominal airgap.

B. Sensitivity to Parameter Errors and Measurement Noise

The sensitivity against parameter errors is analyzed here by means of time-domain simulations. Furthermore, in order to study the measurement-noise amplification of the control system, a noise component (having a maximum peak-to-peak amplitude of 40 μm) is added to the simulated differential airgap Δy. Similarly, a noise component is added to the simulated velocity v_{x}. The amplitudes of the noise components are selected such that they roughly correspond to those seen in the actual measurements in the experimental setup.

The robustness of the control system against parameter errors is evaluated using the same reference-tracking test as in Fig. 7(a). The errors are intentionally introduced in the feedback linearization parameters and in the mover mass [cf. Table I for the original values]. Each parameter value is individually 50% overestimated and 50% underestimated, and the system is simulated. According to the results, the control system remains stable in all the simulations and the reference-tracking accuracy is acceptable. Fig. 8(a) shows the simulation

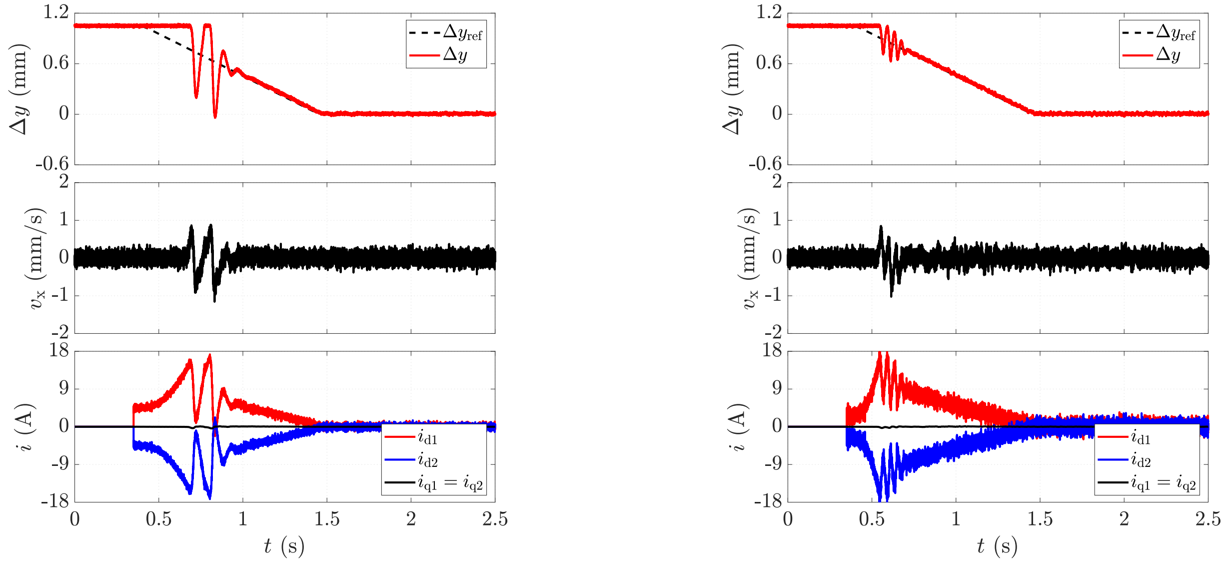

(a) (b)

Fig. 8. Simulation results demonstrating robustness against parameter errors and measurement noise: (a) c_y and f_y are 50% underestimated ($c_y = 0.15$ 1/mm, $f_y = 3.0$ kN); (b) c_y and f_y are 50% underestimated and k_y is 50% overestimated ($c_y = 0.15$ 1/mm, $f_y = 3.0$ kN, $k_y = 195$ N/A). In addition, the control poles are relocated at higher frequencies in (b). In each subfigure, the first subplot shows the measured differential airgap Δy and its reference Δy_{ref}, the second subplot shows the measured x-direction position and velocity, and the last subplot shows the measured currents of the motor units.

result from a test where both c_y and f_y are simultaneously underestimated by 50% (error in the worse direction). Even though the system remains stable, the reference tracking is already severely distorted. If k_x is now 50% overestimated, while keeping c_y, f_y 50% underestimated, then the system becomes unstable. However, the system may be stabilized by relocating the control poles at higher frequencies, e.g., by selecting $\omega_s = 2\pi \cdot 100$ rad/s and $a_p = 2\pi \cdot 10$ rad/s. This is demonstrated with the simulation results in Fig. 8(b). The stabilization comes at the price of increased measurement-noise amplification, which can be clearly seen when comparing the currents in Figs. 8(a) and 8(b).

C. Experimental Tests

There is a risk of having poorly damped structural bending mode of the rail beam in the experimental system (cf. Fig. 5) at the frequency region of 150…200 Hz. In order to prevent from exciting this mechanical resonance, the control poles are shifted to lower frequencies in these preliminary experiments ($\omega_s = 2\pi \cdot 15$ rad/s and $a_p = 2\pi \cdot 1.5$ rad/s). Other control system parameters are selected according to Table I.

Fig. 9 shows results for the reference tracking. The results showing the operation of the upper section are presented Fig. 9(a) and of the lower section in Fig. 9(b). It can be seen that even with the lowered levitation control system bandwidths, a comparatively smooth transition to the stable levitation is achieved for both sections. Moreover, the corresponding simulation results in Fig. 9(c) agree very well with the experiments. Fig. 9(b) shows the results of a test, where the actively levitated mover is travelling 1.3 m in the x direction. The motion starts at $t = 0.25$ s, and the motor units reach the nominal speed $v_x = 1$ m/s during the motion. It can be seen that the levitation controller successfully maintains the stable levitation in the y direction.

VI. Conclusions

A systematic design method for levitation control of a double-sided bearingless linear motor system is presented in this paper. To decouple the force production in thrust- and normal-force directions and to make the levitation-control loop independent of the inner force-control loops, a magnetic-model based feedback-linearization is applied. Then, the design rules for a state-space levitation controller (including the full-order observer) are obtained using pole-placement methods. The proposed control design is tested in an experimental system consisting of four individually supplied linear-motor units in a double-sided configuration. The results from time-domain simulations and experimental tests suggest that the proposed control design can provide smooth transition to contactless operation and to retain the stable levitation during the movement in the thrust-force direction.

References

[1] H.-W. Lee, K.-C. Kim, and J. Lee, "Review of Maglev train technologies," *IEEE Trans. Magn.*, vol. 42, no. 7, pp. 1917–1925, Jul. 2006.

[2] H. Polinder, B. C. Mecrow, A. G. Jack, P. G. Dickinson, and M. A. Mueller, "Conventional and TFPM linear generators for direct-drive wave energy conversion," *IEEE Trans. Energy Convers.*, vol. 20, no. 2, pp. 260–267, Jun. 2005.

[3] D. Patterson, A. Monti, C. W. Brice, R. A. Dougal, R. O. Pettus, S. Dhulipala, D. C. Kovuri, and T. Bertoncelli, "Design and simulation of a permanent-magnet electromagnetic aircraft launcher," *IEEE Trans. Ind. Appl.*, vol. 41, no. 2, pp. 566–575, Mar./Apr. 2005.

[4] L. Huang, H. Yu, M. Hu, and H. Liu, "Study on a long primary flux-switching permanent magnet linear motor for electromagnetic launch systems," *IEEE Trans. Plasma Sci.*, vol. 41, no. 5, pp. 1138–1144, May 2013.

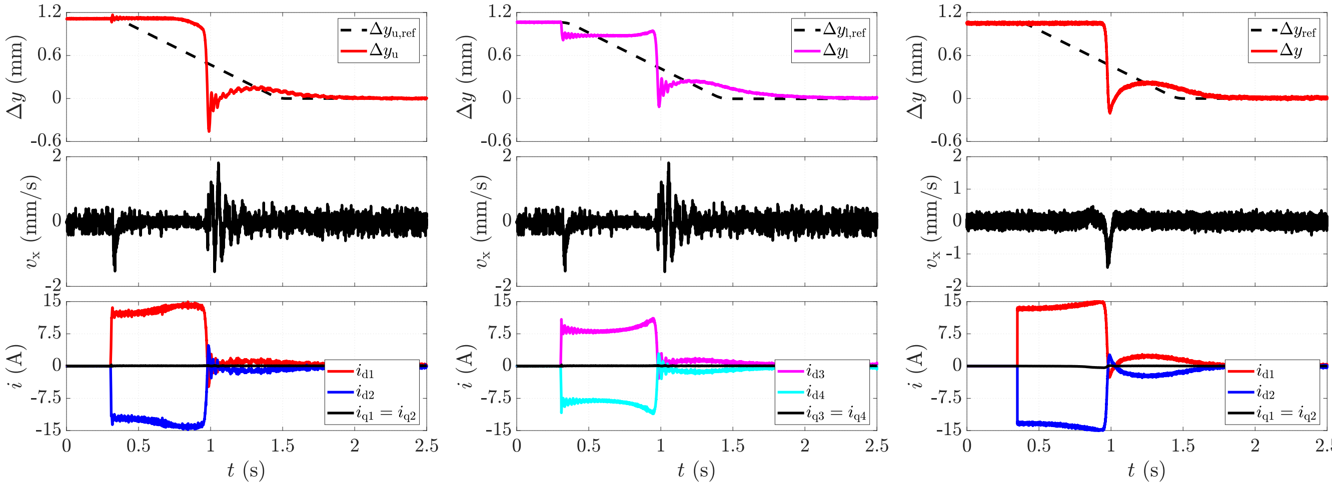

(a) (b) (c)

Fig. 9. Experimental results for the proposed levitation controller: (a) upper section; (b) lower section; (c) simulation results as a reference. Active levitation starts at $t = 0.3$ s. Motor units 2 and 4 are initially attached to the rail. In each subfigure, the first subplot shows the measured differential airgap together with the reference, the second subplot shows the measured x-direction position and velocity, and the last subplot shows the measured currents.

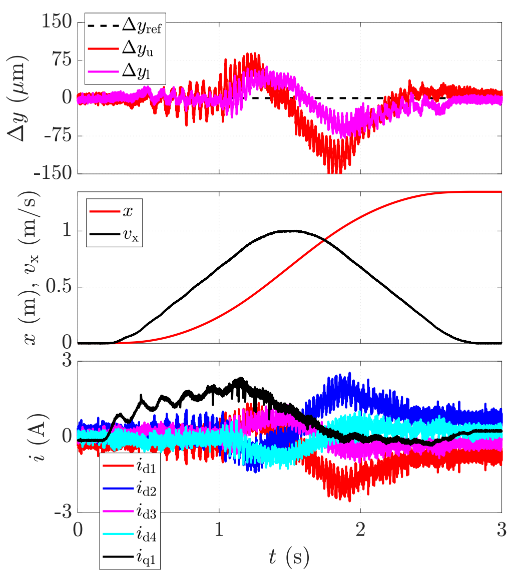

Fig. 10. Experimental results, where the levitated mover travels 1.3 m on the rail. The motion starts at $t = 0.25$ s. The first subplot shows the measured differential airgaps together with the reference, the second subplot shows the measured x-direction position and velocity, and the last subplot shows the measured currents of the motor units.

[5] S. Gordon and M. T. Hillery, "Development of a high-speed CNC cutting machine using linear motors," *Journal of Materials Processing Technology*, vol. 166, no. 3, pp. 321–329, Aug. 2005.

[6] I. Petrov, T. Purosto, T. Hakala, and J. Ratia, "Electric linear motor," 2016, *Patent Application WO 2016/207136 A1*.

[7] B. Zhang, M. Cheng, S. Zhu, M. Zhang, W. Hua, and R. Cao, "Investigation of linear flux-switching permanent magnet machine for ropeless elevator," in *Proc. ICEMS*, Chiba, Japan, Nov. 2016.

[8] E. Lantto, "Robust control of magnetic bearings in subcritical machines," D.Sc. dissertation, Helsinki University of Technology, Espoo, Finland, 1999.

[9] R. L. Fittro and C. R. Knospe, "The μ approach to control of active magnetic bearings," *J. Eng. Gas Turbines Power*, vol. 124, no. 3, pp. 565–570, Jun. 2002.

[10] J. D. Lindlau and C. R. Knospe, "Feedback linearization of an active magnetic bearing with voltage control," *IEEE Trans. Control Syst. Technol.*, vol. 10, no. 1, pp. 21–31, Jan 2002.

[11] R. P. Jastrzebski and R. Pöllänen, "Centralized optimal position control for active magnetic bearings: comparison with decentralized control," *Electr. Eng.*, vol. 91, no. 2, pp. 101–114, Aug. 2009.

[12] T. Schuhmann, W. Hofmann, and R. Werner, "Improving operational performance of active magnetic bearings using Kalman filter and state feedback control," *IEEE Trans. Ind. Electron.*, vol. 59, no. 2, pp. 821–829, Feb. 2012.

[13] I. Takahashi and Y. Ide, "Decoupling control of thrust and attractive force of a LIM using a space vector control inverter," *IEEE Trans. Ind. Appl.*, vol. 29, no. 1, pp. 161–167, Jan./Feb. 1993.

[14] M. Ooshima, A. Chiba, A. Rahman, and T. Fukao, "An improved control method of buried-type IPM bearingless motors considering magnetic saturation and magnetic pull variation," *IEEE Trans. Energy Convers.*, vol. 19, no. 3, pp. 569–575, Sep. 2004.

[15] G. Valente, A. Formentini, L. Papini, C. Gerada, and P. Zanchetta, "Performance improvement of bearingless multisector PMSM with optimal robust position control," *IEEE Trans. Power Electron.*, vol. 34, no. 4, pp. 3575–3585, Apr. 2019.

[16] W. Kim, J. M. Lee, and S. Kim, "Rolling motion control of a levitated mover in a permanent-magnet-type bearingless linear motor," *IEEE Trans. Magn.*, vol. 46, no. 6, pp. 2482–2485, Jun. 2010.

[17] W. Gruber, M. Rothböck, and R. T. Schöb, "Design of a novel homopolar bearingless slice motor with reluctance rotor," *IEEE Trans. Ind. Appl.*, vol. 51, no. 2, pp. 1456–1464, Mar./Apr. 2015.

[18] D.-J. Bang and S.-H. Hwang, "Wide air-gap control for multi-module permanent magnet linear synchronous motors without magnetic levitation windings," *Journal of Power Electronics*, vol. 16, no. 5, pp. 1773–1780, Sep. 2016.

[19] R. P. Jastrzebski, P. Jaatinen, and O. Pyrhönen, "Modeling and control design simulations of a linear flux-switching permanent-magnet-levitated motor," *Mechanical Engineering Journal*, vol. 4, no. 5, Jul. 2017.

[20] M. Sokolov, S. E. Saarakkala, R. Hosseinzadeh, and M. Hinkkanen, "Modeling of a bearingless flux-switching permanent-magnet linear motor," in *Proc. IEEE ITEC*, Long Beach, CA, Jun. 2018, pp. 851–857.

[21] L. Harnefors and H. P. Nee, "Model-based current control of AC machines using the internal model control method," *IEEE Trans. Ind. Appl.*, vol. 34, no. 1, pp. 133–141, Jan./Feb. 1998.